

Diffusion-based Method for Satellite Pattern-of-Life Identification

Yongchao Ye^{1*}, Xinting Zhu^{1*}, Xuejin Shen², Xiaoyu Chen², Lishuai Li^{1†}, S. Joe Qin³

¹Department of Data Science, City University of Hong Kong, Hong Kong SAR, China

²Chengdu Atom Data Tech Co., Ltd, Chengdu, China

³School of Data Science, Lingnan University, Hong Kong SAR, China

yongchao.ye@my.cityu.edu.hk, xt.zhu@my.cityu.edu.hk, xuejin.shen@starinnov.com

seanchen@outlook.com, lishuai.li@cityu.edu.hk, joeqin@ln.edu.hk

Abstract

Satellite pattern-of-life (PoL) identification is crucial for space safety and satellite monitoring, involving the analysis of typical satellite behaviors such as station-keeping, drift, etc. However, existing PoL identification methods remain underdeveloped due to the complexity of aerospace systems, variability in satellite behaviors, and fluctuating observation sampling rates. In a first attempt, we developed a domain expertise-informed machine learning method (Expert-ML) to combine satellite orbital movement knowledge and machine learning models. The Expert-ML method achieved high accuracy results in simulation data and real-world data with normal sampling rate. However, this approach lacks of generality as it requires domain expertise and its performance degraded significantly when data sampling rate varied. To achieve generality, we propose a novel diffusion-based PoL identification method. Distinct from prior approaches, the proposed method leverages a diffusion model to achieve end-to-end identification without manual refinement or domain-specific knowledge. Specifically, we employ a multivariate time-series encoder to capture hidden representations of satellite positional data. The encoded features are subsequently incorporated as conditional information in the denoising process to generate PoL labels. Through experimentation across real-world satellite settings, our proposed diffusion-based method demonstrates its high identification quality and provides a robust solution even with reduced data sampling rates, indicating its great potential in practical satellite behavior pattern identification, tracking and related mission deployment.

Keywords: Satellite Pattern-of-life, Space Situational Awareness, Diffusion Model

1 Introduction

With the increasing number of space objects operating in Earth’s vicinity, space situational awareness (SSA) technology has become more crucial than ever for tracking and predicting orbital maneuvers, ensuring safe and sustainable space operations. According to global statistics on orbiting

* These authors contributed equally to this work.

† Corresponding author.

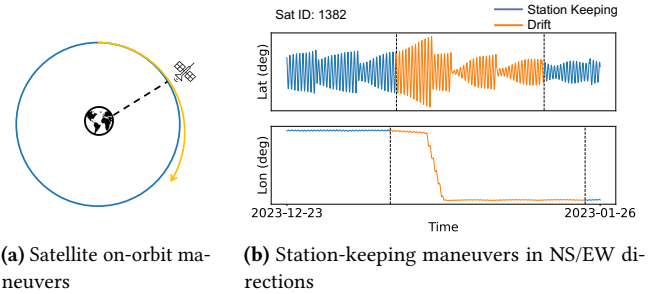


Figure 1. Example of pattern-of-life behavior of a GEO satellite in station-keeping maneuvers.

satellite objects, approximately 26,700 satellites were circling Earth by 2023, marking a 6.8% increase from the previous year [24]. This growth has led to an increased probability of object collisions and potential disasters.

In SSA, one effective approach is tracking and characterizing on-orbit satellite pattern-of-life (PoL) behaviors [20, 21]. Satellite PoL refers to the typical behaviors and operational modes of satellites as operators issue commands for different mission types, such as station-keeping [10], longitudinal-shift maneuvers [20], and retirement maneuvers [14]. For instance, station-keeping maneuvers, a primary behavior in geostationary equatorial orbit (GEO) satellite operations, are performed to maintain the satellite’s position within a designated orbital slot, counteracting perturbations such as gravitational influences from the sun and moon, and the irregular shape of the Earth [11]. Station-keeping maneuvers can be further classified into north-south (NS) and east-west (EW) types, referring to corrections in geographic latitude and longitude, respectively. Fig. 1 illustrates an example of GEO satellite PoL station-keeping behaviors over a specific period. Identifying these behavioral modes allows for a better understanding of satellite operational patterns, improving tracking capabilities, and more effective mission planning and satellite management strategies.

However, identifying satellite PoL encounters several significant challenges in practice. First, due to the complexity of aerospace systems like satellites, commonly adopted rule-based or statistical methods rely heavily on extensive expert

knowledge [12, 18, 37], making them labor-intensive and human overload with the blooming number of daily generated operational data and limiting their scalability with increasing satellites to track and applicability across different satellites and systems. Second, the behaviors of different satellites can vary greatly because of not common control strategies and also propulsion types, posing challenges in modeling and predicting individual on-orbit behavior patterns. While there have been efforts to use supervised learning and deep neural networks [19, 22], the outputs of these models often require further refinement to produce a usable PoL sequence. These challenges are also present in similar sequence segmentation problems, such as action segmentation [13, 29] and time-series segmentation [2, 17], where accurately delineating sequences is crucial. Third, another typical issue in identifying satellite PoL behaviors is the variations in the sampling rate of satellite observation data. Due to different surveillance requirements for different objects and signal transmission issues in practice, the sampling resolution fluctuates among different objects and different periods. These fluctuations lead to incomplete or inconsistent series, making it difficult to develop generic PoL identification algorithms to maintain accuracy and reliability across different conditions. For example, in our another attempt, we found that physical rule-based machine learning methods had good accuracy but showed deployment failures in practice when the observation frequency was inconsistent, which is further discussed in Sec. 3.

To address the existing gaps, we propose a diffusion-based segmentation method for satellite PoL identification, DiffPoL, which effectively learns the complex patterns among various satellites and achieves end-to-end PoL identification. Inspired by previous studies [3, 13, 16], we design this method based on the following primary motivations: (1) Compared to rule-based methods, data-driven models generally exhibit better generalization across different satellites and systems, and are more robust to variations in data sampling rates. (2) Existing segmentation methods often employ step-by-step refinement [13], whereas the diffusion model denoises step-by-step from white noise to achieve the final result, potentially enabling end-to-end identification [16].

While the diffusion model shows powerful modeling ability in various sequences modeling tasks [28, 35], it poses a non-trivial challenge when applied to satellite PoL identification. Firstly, satellite PoL identification is not a standard conditional generation problem, necessitating the adaptation of the diffusion model. Secondly, the position sequences of satellites constitute a multivariate time series, requiring the model to simultaneously consider dependencies across both temporal and feature dimensions. Addressing these challenges is crucial for successfully applying the diffusion model to satellite PoL identification and ensuring accurate, robust outcomes.

Building on the identified motivations and addressing the existing gaps, we propose a diffusion-based segmentation method for satellite PoL identification, DiffPoL, which resolves the satellite PoL identification problem as a conditional PoL sequence generation task. DiffPoL incorporates a multivariate time-series encoder that captures the hidden representation of satellite positional observations. This representation is subsequently applied as conditional information in the denoising process and fed into a tailor-made decoder to generate the PoL sequence. In summary, the contributions of this research are as follows:

- We propose a diffusion-based method for satellite PoL identification. To the best of our knowledge, this is the first exploration of satellite PoL identification using the diffusion model.
- We validate the effectiveness of DiffPoL on real-world satellite datasets and prove its powerful denoising capabilities to achieve accurate end-to-end PoL identification without the need of manual refinement or domain-specific knowledge.
- We demonstrate the scalability and applicability of DiffPoL by comparing it with current practices, and also verify its robustness on the different sampling rates which is a common challenge in satellite behavior surveillance.

2 Preliminaries

2.1 Problem Definition

Satellite Position: Satellite position can be represented as a multivariate time series, denoted as $\mathbf{x} = \{p_t | t = 1, \dots, T\}$, where p_t is the position at a given time t , and T is the length of the sequence. Each position p_t is a d -dimensional vector that records the satellite’s location and movement in specific coordinate systems. Typical coordinate systems include six Keplerian elements, geodetic coordinates (latitude, longitude, and altitude - LLA), and standard equatorial coordinate position and velocity vectors [26].

Satellite PoL: Satellite pattern-of-life (PoL) refers to the behavior of a satellite over time, encompassing various operational activities and maneuvers. Specifically, this study focuses on the station-keeping behaviors of GEO satellites in the EW and NS directions. Following the definition in previous studies [21], the station-keeping maneuvers are divided into three categories based on the propulsion system used: electric propulsion (EK), chemical propulsion (CK), and hybrid propulsion (HK). Non-station-keeping behaviors are divided into initial drift (ID) and adjust drift (AD), where ID represents a satellite that leaves the desired orbit and starts drifting, and AD refers to any significant changes in longitude drift rate or direction for a drifting satellite. Note that identification in EW and NS directions is independent, as EW and NS maneuvers correspond to different physical operations.

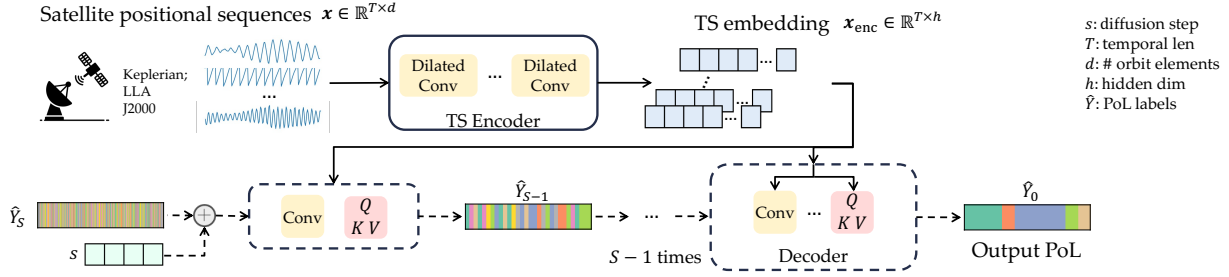


Figure 2. The overview of the proposed identification framework. A time-series encoder first encodes satellite positional sequences into high-dimensional embeddings. Then embeddings are fed into the decoder as conditional information in the denoising process via cross-attention.

Problem Statement (Satellite PoL Identification): The objective of satellite PoL identification is to determine the maneuvers of the satellite at each timestamp. In other words, it is a sequence labeling problem where the goal is to predict the PoL label for each timestamp in the satellite position sequence. Formally, the task is to learn a function $f: \mathbf{x} \rightarrow \hat{Y}$ that maps each position sequence \mathbf{x} to a sequence of PoL labels \hat{Y} , where $\hat{Y} = \{\hat{y}_t | t = 1, \dots, T\}$ and $\hat{y}_t \in \mathcal{A}$, with $\mathcal{A} = \{\text{ID, AD, EK, CK, HK}\}$ representing the set of PoL classes. The aim is to minimize the error between the prediction \hat{Y} and the true PoL labels Y . To ensure the high utility of the sequence labels, the prediction should not only have high point-wise accuracy at each timestamp but also perform well on the sequence level.

2.2 Conditional Diffusion Probabilistic Model

Diffusion probabilistic models have achieved state-of-the-art performance in various domains [7, 31], and their performance is further enhanced when conditioned on specific information [15, 34, 36]. Typical diffusion models comprise two processes: the forward (diffusion) process that gradually corrupts the original data into Gaussian noise, and the reverse (denoising) process that aims to recover the original data from the noise.

Forward Process. The forward process aims to transform the original data into a Gaussian noise distribution by sequentially adding noise. Formally, this process can be represented as a Markov chain that transforms the original data $\mathbf{x}_0 \sim q(\mathbf{x}_0)$ into a series of noisy data $\mathbf{x}_1, \mathbf{x}_2, \dots, \mathbf{x}_S$, where $\mathbf{x}_S \sim \mathcal{N}(0, \mathbf{I})$. At each diffusion step s , noise is added according to the equation:

$$q(\mathbf{x}_s | \mathbf{x}_{s-1}) = \mathcal{N}(\mathbf{x}_s; \sqrt{1 - \beta_s} \mathbf{x}_{s-1}, \beta_s \mathbf{I}), \quad (1)$$

where β_s is a variance schedule that controls the amount of noise added at each step. For gradient-based optimization, the reparameterization trick is applied to efficiently sample from this distribution [8], allowing us to obtain the noisy data \mathbf{x}_s without recursion from \mathbf{x}_0 ,

$$\mathbf{x}_s = \sqrt{\bar{\alpha}_s} \mathbf{x}_0 + \epsilon \sqrt{1 - \bar{\alpha}_s}, \quad (2)$$

where $\epsilon \sim \mathcal{N}(0, \mathbf{I})$, and $\bar{\alpha}_s = \prod_{i=1}^s (1 - \beta_i)$.

Reverse Process. The reverse process recovers the original data distribution from a Gaussian noise state. It starts from \mathbf{x}_S and progressively denoises the data using learned parameters. At each diffusion step s , the model predicts the mean and variance of the data distribution at the previous diffusion step $s - 1$ conditioned on the current noisy data \mathbf{x}_s and some conditional information \mathbf{c} . The conditional reverse process is described by the equation:

$$p_\theta(\mathbf{x}_{s-1} | \mathbf{x}_s, \mathbf{c}) = \mathcal{N}(\mathbf{x}_{s-1}; \mu_\theta(\mathbf{x}_s, \mathbf{c}, s), \sigma_\theta^2(\mathbf{x}_s, \mathbf{c}, s) \mathbf{I}), \quad (3)$$

where $\mu_\theta(\mathbf{x}_s, \mathbf{c}, s)$ and $\sigma_\theta^2(\mathbf{x}_s, \mathbf{c}, s)$ are the mean and variance at reverse step s , respectively. Both μ_θ and σ_θ are parameterized by θ and modulated by the conditional information \mathbf{c} . In this study, μ_θ and σ_θ are estimated by a neural network $f_\theta(\mathbf{x}_s, \mathbf{c}, s)$ to model the mean and variance functions, which are trained by minimizing the loss, $\mathcal{L} = \|f_\theta(\mathbf{x}_s, \mathbf{c}, s), \mathbf{x}_0\|$ [23].

The inference stage starts from the Gaussian noise state at the final step $\mathbf{x}_S \sim \mathcal{N}(0, \mathbf{I})$, and then gradually denoises the data with the trained module f_θ [23],

$$\mathbf{x}_{s-1} = \sqrt{\bar{\alpha}_{s-1}} f_\theta(\mathbf{x}_s, \mathbf{c}, s) + \frac{\sqrt{1 - \bar{\alpha}_{s-1}} \sigma_\theta^2 \mathbf{x}_s - \sqrt{\bar{\alpha}_s} f_\theta(\mathbf{x}_s, \mathbf{c}, s)}{\sqrt{1 - \bar{\alpha}_s}} + \sigma_s \epsilon. \quad (4)$$

This iteration can be accelerated by skipping strategy [23].

3 Expert-ML method for PoL identification

We first introduce our domain expertise-informed machine learning method, Expert-ML, for satellite PoL identification. Expert-ML method is a combination of rules based on domain knowledge of celestial motion and data-driven models, differentiating the identification in EW and NS direction due to their independent operations and maneuvers. Specifically, rule-based methods are designed based on empirical observations, e.g., step changes in eccentricity represent a part of maneuvers in EW direction [11]. And data-driven models are trained with critical orbital elements, e.g., a projection in equinoctial coordinates for NS direction [26]. Finally, identifications are refined by cross-verifying and addressing exceptional cases. The performance of Expert-ML ranks 6 out of

over 30 participant teams in the satellite PoL identification challenge.

Although Expert-ML can achieve competitive PoL identification, it has limitations in algorithm design and actual deployment. First, rules are defined based on observations from the data and expert knowledge, which need to be manually updated when applied to different satellites and are particularly sensitive to positional sequences with low sampling rates. Second, despite using some data-driven methods, these simple machine learning models rely on feature engineering, which is based on expert knowledge. The design of feature engineering may vary for different satellites. Third, since neither rule-based nor data-driven methods can directly achieve satisfactory PoL identification, complex rules are defined to refine outputs from different methods. Details of Expert and discussion can be found in **Appendix A**.

4 Diffusion-based Method for PoL identification

In this section, we introduce the workflow of the proposed DiffPoL, which identifies PoL in a point-wise sequence generation manner. The overview of DiffPoL is illustrated in Fig. 2. The method begins with a time-series encoder that takes multi-variate satellite positional sequences as input and embeds them into a high-dimensional time-series representation. Subsequently, in the denoising process, marked with dashed arrows, the embeddings are utilized as conditional information. The embedding, together with random noise, is fed into a decoder to gradually refine the noise to the PoL label sequence. The encoder consists of multiple dilated convolutional layers, and the denoising is achieved by a decoder with dilated convolutional layer and cross-attention mechanism, which are detailed in the following subsections.

4.1 Encoder structure

The encoder aims to learn hidden representations of the satellite sequences, which is crucial for accurate PoL identification. The learned representations, which are utilized as conditional information in the denoising process, should encapsulate the temporal patterns and positional characteristics of the satellite sequences. As the satellite positional sequences are multi-variate and exhibit complex temporal patterns, we follow those well-developed modules in time-series representation learning [32, 33] and design a multi-layered encoder structure.

The encoder structure of the proposed model, depicted in Fig. 3, consists of a series of dilated convolutional blocks as the backbone. The input of the encoder is the multi-variate satellite positional sequences, $\mathbf{x} \in \mathbb{R}^{T \times d}$, where T is the temporal period length and d is the number of orbit elements. The satellite positional sequence \mathbf{x} is first passed through a fully connected (FC) layer to perform an initial transformation on the feature dimension. Next, the transformed

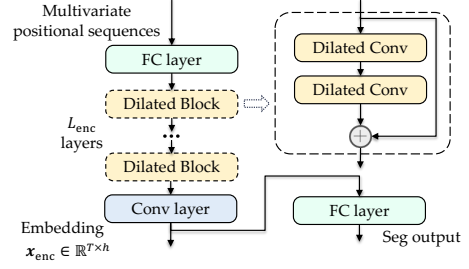


Figure 3. The encoder structure. Dilated convolutional layers are applied to learn hierarchical temporal patterns.

sequences are fed into L_{enc} layers of dilated convolutional blocks. Each dilated block consists of two dilated convolutional layers, which are crucial for capturing long-range dependencies within the time-series data. Mathematically, a dilated convolution with filter $\omega \in \mathbb{R}^K$ can be defined as:

$$(\mathbf{x} *_d \omega)(t) = \sum_{i=0}^{K-1} \omega(i) \mathbf{x}(t - i \times d), \quad (5)$$

where x is the input sequence, k is the convolutional kernel size, and d is the dilation factor. With d , which controls the skipping distance of the convolution operation, the convolutional kernel picks inputs every d step and applies the standard 1D convolution to the selected inputs. The dilation factor increases exponentially with the depth of the dilated blocks, allowing the network to capture hierarchical temporal patterns without a significant increase in computational cost. In this study, we set $d = 2^l$, where l is the layer index of dilated blocks. Additionally, a residual connection is applied in each block to facilitate the training process and prevent the vanishing gradient problem.

After passing through L_{enc} layers of dilated blocks, the features are concatenated and processed by another convolutional layer to further refine the embeddings to the desired output dimension. The output of this convolutional layer is a set of time-series embeddings, $\mathbf{x}_{enc}^{T \times h}$, which encapsulate the temporal dynamics and positional information of the satellite and are fed into the decoder as conditional information in the denoising process.

Additionally, inspired by the design in the previous study [16], we include an extra output from the encoder. It is processed by a fully connected (FC) layer, which maps the embeddings to the class dimension. During training, this output is supervised using a cross-entropy loss, serving as an auxiliary loss to aid in model training, though it is not utilized during the inference process.

4.2 Decoder structure

As introduced in Sec. 2.1, the denoising process is achieved by a neural network module $f_{\theta}(\mathbf{x}_s, \mathbf{c}, s)$ that predicts label sequence Y_0 at a given diffusion step s with the noised state \mathbf{x}_s and the conditional information \mathbf{c} . The step-by-step denoising paradigm is similar to the sequence-level refinement

in traditional segmentation methods [3, 13]. However, while those methods rely on different network designs or manually crafted rules, the denoising process can achieve this refinement in an end-to-end manner.

In this study, we customize the decoder structure and identify PoL labels in a point-wise sequence generation way. Specifically, each diffusion state is a noised PoL label sequence \hat{Y}_s , and the embedding of the positional sequence \mathbf{x}_{enc} is utilized as conditional information c . The decoder structure of the proposed model, illustrated in Fig. 4, utilizes a combination of convolutional and cross-attention blocks. Inputs of the decoder are grouped into two-fold: the noised PoL label sequence Y_s combined with the diffusion step s , and the conditional information \mathbf{x}_{enc} . The diffusion step s is first embedded into the same dimension as the noised state \hat{Y}_s with sinusoidal embedding [25], and then concatenated with the noised state, denoted as h_s . The embedding from the encoder first passes through a convolutional layer, denoted as h_c .

Subsequently, the decoder incorporates L_{dec} layers of cross-attention blocks. Each cross-attention block includes a dilated convolution layer, which captures hierarchical dependencies within the embedding from the encoder. Additionally, cross-attention mechanisms are applied to integrate the conditional information from the encoder and the noised state.

$$Q = W_q \cdot (h_c \oplus h_s), K = W_k \cdot (h_c \oplus h_s), V = W_v \cdot \text{Conv}(h_c), \quad (6)$$

where h_c is the conditional embedding, h_s is the state embedding, and W_q, W_k, W_v are learnable weight matrices. Then, the output of cross-attention is calculated as: $h = \text{softmax}(\frac{Q \cdot K^T}{\sqrt{d_k}}) \cdot V$. To prevent overfitting and improve generalization, dropout layers are applied before and after the dilated convolution operations.

Finally, the refined embeddings from the cross-attention blocks are passed through a final convolutional layer, which maps the learned features to PoL classes. And a softmax layer is applied to calculate the probability at each time step over different PoL categories, $p_i = \text{softmax}(\frac{e^{z_i}}{\sum_C e_i^z})$. This output, i.e., the denoised sequence, $p \in \mathbb{R}^{T \times C}$ represents the PoL labels \hat{Y}_s , indicating the identified behaviors of the satellite over time.

4.3 Training and inference

With the introduced encoder and decoder structures, the diffusion model generates PoL label sequence based on the noised state and the conditional information. The training and inference processes of the proposed model are detailed in Algorithm 1.

Training process: The training process begins by embedding the positional sequence x into \mathbf{x}_{enc} using the encoder θ_{enc} . Then, we apply the condition masking strategy in literature [16] to control the conditional information [9]. Next,

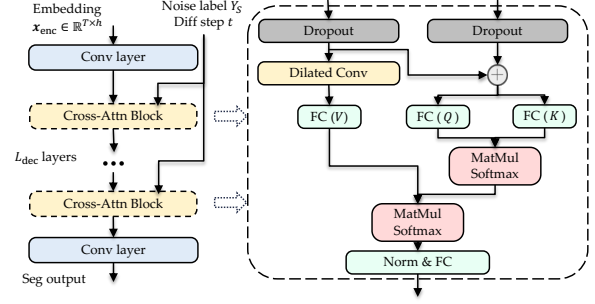


Figure 4. The decoder structure. Cross-attention block is designed to integrate embedding and noised state.

Algorithm 1 Train and inference processes of DiffPoL

Training Process:

- 1: **for** $i = 1, 2, \dots$, **do**
- 2: Positional sequence \mathbf{x} , PoL label Y
- 3: Get embedding \mathbf{x}_{enc} from the encoder θ_{enc}
- 4: Get masked embedding $\mathbf{x}_{\text{enc}} = \mathbf{x}_{\text{enc}} \odot M$
- 5: Sample Y_0 from label distribution $q(Y)$,
- 6: Sample diffusion step $s \sim \text{Uniform}(\{1, \dots, S\})$,
- 7: $\epsilon \sim \mathcal{N}(0, \mathbf{I})$
- 8: $Y_s = \sqrt{\alpha_s} Y_0 + \epsilon \sqrt{1 - \alpha_s}$
- 9: Denoise with the decoder θ_{dec} , $\hat{Y}_0 = f_{\theta_{\text{dec}}}(Y_s, \mathbf{x}_{\text{enc}}, s)$
- 9: Update gradient $\nabla \theta_{\text{enc}}, \nabla \theta_{\text{dec}}$, with loss
- $\mathcal{L} = \mathcal{L}_{ce} + \mathcal{L}_{smo} + \mathcal{L}_{bd}$

Inference Process:

- 11: Positional sequence \mathbf{x}
- 12: Get embedding \mathbf{x}_{enc} from the encoder θ_{enc}
- 13: Sample $\hat{Y}_s \sim \mathcal{N}(0, \mathbf{I})$
- 14: **for** $s = S, S - \nabla s, \dots, 1$ **do**
- 15: Compute \hat{Y}_s according to Eq. (4)
- 16: **end for**
- 17: **return** \hat{Y}_0

for a diffusion step s , a noised PoL label sequence y_s is sampled. The decoder denoises \hat{y}_s to predict \hat{y}_0 by leveraging the conditional information from \mathbf{x}_{enc} . The encoder and decoder are optimized jointly with a combined loss function L , which are detailed as follows.

Cross-Entropy Loss: Conventional cross-entropy loss is applied as point-wise supervision, which minimizes the negative log-likelihood of the ground truth PoL class for each timestep. The cross-entropy loss \mathcal{L}_{ce} is defined as:

$$\mathcal{L}_{ce} = -\frac{1}{TC} \sum_T \sum_C Y_{t,c} \log p_{t,c} \quad (7)$$

where T is the temporal length, C is the number of PoL categories, Y is the ground truth label, and $p_{t,c}$ is the predicted probability for class c at time step t .

Smooth Loss: A smooth loss is applied to maintain consistency in predictions over consecutive frames. The loss

\mathcal{L}_{smo} is calculated by minimizing the difference in the log-likelihoods between adjacent frames [5, 13]:

$$\mathcal{L}_{smo} = \frac{1}{(T-1)C} \sum_{T-1} \sum_C (\log p_{t,c} - \log p_{t+1,c})^2 \quad (8)$$

Boundary Alignment Loss: Identifying the transition boundaries between different PoL classes is crucial for PoL identification, as well as other sequence segmentation tasks. The boundary probabilities are computed by taking the dot product of the action probabilities from neighboring frames in p_s , and the alignment is achieved using a binary cross-entropy loss. The boundary alignment loss \mathcal{L}_{bd} is defined as [16]:

$$\mathcal{L}_{bd} = \frac{1}{T-1} \sum_{T-1} [-\bar{B}_t \log(1 - p_t \cdot p_{i+1}) - (1 - \bar{B}_t) \log(p_t \cdot p_{i+1})] \quad (9)$$

where $\bar{B} \in \mathbb{B}^T$ is the smoothed boundary sequence derived from the ground truth.

Inference process: As described in Algorithm 1, the inference process is guided by the learned representation x_{enc} from the encoder. The initial noisy PoL label sequence \hat{y}_S is generated by sampling from a Gaussian distribution $\mathcal{N}(0, I)$. Subsequently, the model iterates through each diffusion step, starting from S down to 1. At each step s , the decoder utilizes the current noisy PoL label \hat{y}_s , the conditional embedding x_{enc} , and the diffusion step information to refine the sequence according to Eq. (4). The denoising process progressively reduces the noise, moving closer to the ground truth.

5 Experiments

We conduct comprehensive experiments on a thorough satellite dataset to show the superior performance of the proposed DiffPoL in PoL identification. This section only includes the basic setup, comparison of the main experimental results, and visualization results. Owing to space limitations, detailed settings, more results and ablation studies are reported in the Appendix.

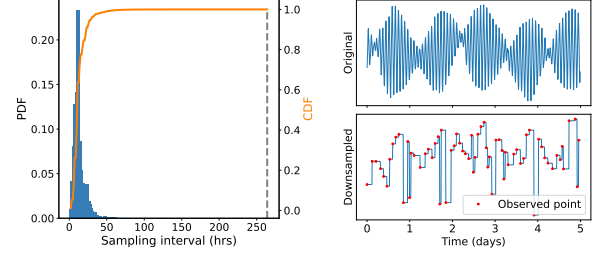
5.1 Settings

5.1.1 Dataset. We evaluate DiffPoL on the Satellite Pattern-of-Life Identification Dataset (SPLID), designed by MIT ARCLab to support satellite behavior characterization studies¹. The dataset contains both synthetic data generated by a high-fidelity satellite simulation tool and real-world data derived from satellite tracking records [21]. The position is recorded every two hours with 15 orbital parameters, including orbital elements, geodetic positions and J2000 position and velocity. PoL labels in EW and NS directions are provided for each satellite, details are summarized in Table 1.

In addition to the original dataset, we consider a more realistic scenario where satellite positions cannot be observed

Table 1. SPLID dataset statistics

Direction	# Object	# Period	# PoL label	# Transition / Object
EW	1900	6 month	5	1.69
NS			4	1.13



(a) PDF and CDF of the low sampling interval. The average interval is 13.7 quences (Eccentricity) with low sampling rate.

Figure 5. Positional sequences with low sampling rate.

at regular intervals due to various factors such as different satellite mission types, signal transmission issues, solar storms, etc. Such scenarios pose challenges when deploying PoL algorithms, as the reduced sampling rate may lead to incomplete positional sequences, affecting the identification performance. In Fig. 5a, we present the Probability Density Function (PDF) and Cumulative Distribution Function (CDF) of satellite position data sampling intervals in real-world scenarios. The sampling interval distribution shows that most intervals are concentrated in a short time range (~ 12 hours), but there are also instances of significantly longer intervals (more than 7 days), indicating substantial variability in sampling rates. Fig. 5b illustrates an example of a positional sequence with both original and low sampling rates. The red dots represent the observed positions, and the sequence is imputed to its original sampling rate using forward padding. It is evident that the reduced sampling rate severely truncates the original positional sequence, resulting in a markedly different time-series pattern. Thus, we evaluate the PoL identification performance with both original and low sampling rate positional sequences.

5.1.2 Evaluation metrics. To fully evaluate the quality of PoL identification, we follow the practice in sequence segmentation tasks [3, 16], and use three evaluation metrics at different levels: **Accuracy (Acc)** is a point-wise metric that measures the proportion of correctly identified PoL labels out of the total labels. **Edit score (Edit)** is a sequence-level metric that quantifies the similarity between two sequences based on the Levenshtein distance, which is the minimum number of actions required to transform one sequence into another. **F1-score (F1)** is a segment-level metric that compares the Intersection over Union (IoU) of each segment with respect to the corresponding ground truth based on a threshold τ . Details of the evaluation metrics are provided in **Appendix B**.

¹<https://eval.ai/web/challenges/challenge-page/2164/overview>

Table 2. Performance Comparison of DiffPoL and baseline methods in EW and NS directions.

Method	EW direction			NS direction		
	F1 (%) @ {10,25,50} (↑)	Edit (%) (↑)	Acc (%) (↑)	F1 (%) @ {10,25,50} (↑)	Edit (%) (↑)	Acc (%) (↑)
Heuristic	24.46 / 22.34 / 21.86	59.19	38.83	43.18 / 39.17 / 32.49	37.06	38.41
CLaSP	28.66 / 20.47 / 11.69	24.91	41.66	36.66 / 26.72 / 14.07	37.07	42.23
RF	42.02 / 41.71 / 40.88	74.82	95.50	34.30 / 33.96 / 33.11	70.55	95.60
CNN	39.39 / 34.02 / 27.51	41.13	76.43	58.50 / 57.54 / 54.52	66.40	91.55
TS2Vec	19.61 / 18.98 / 17.80	68.73	88.61	23.61 / 23.18 / 22.40	56.52	95.03
Expert-ML	93.92 / 93.71 / 93.40	93.79	92.94	95.69 / 95.19 / 93.69	93.97	95.21
DiffPoL	91.68 / 91.00 / 89.92	93.00	94.10	94.79 / 94.67 / 94.08	96.72	98.20

Bold indicates the best performance over the baselines. ↑: higher is better.

5.1.3 Implementation details. In this study, positional records of 1900 satellites are applied. We select six Keplerian elements and geodetic positions as input features, which are 9-dimension time-series sequences. During the training stage, the dataset is randomly divided into training and testing sets with a ratio of 80% and 20%, respectively. As maneuvers in EW and NS directions correspond to motion states, we treat PoL identification in the EW and NS directions as two separate tasks.

For the model hyperparameters, 9 layers of dilated convolutional blocks are concatenated in the encoder, with a hidden dimension of 64 and an initial dilation rate of 2. The convolutional kernel size is set to 12 to capture the daily periodicity of the satellite. For the decoder, 3 layers of cross-attention and convolutional blocks are stacked, with a hidden dimension of 64. The dropout rate is set to 0.1 for both the encoder and decoder. The smooth loss is clipped to avoid outlier values, ensuring the smoothness of the predicted sequence [13, 16]. The encoder and decoder are trained in an end-to-end manner using the Adam optimizer with a batch size of 4. The learning rate is initialized at $5e-4$ and decayed with a rate at $1e-5$. The number of diffusion steps is set to 1000, with 25 steps utilized at inference based on a sampling strategy with skipped steps. All experiments are implemented in PyTorch and conducted on a server with NVIDIA A30 GPU. The implementation is available for reproducibility ².

5.2 Baselines

We compare the proposed method **DiffPoL** and previously designed method **Expert-ML** with the following baselines.

- **Heuristic:** [21] A heuristic method is developed along with the satellite PoL dataset, which is a combination of rules based on satellite maneuvers.
- **CLaSP:** [4] CLaSP is an unsupervised change point detection method for invariant time-series data. We select longitude and inclination and apply CLaSP for EW and NS detection, respectively.

- **Random Forest (RF):** We apply a 7-day sliding window on the positional sequences and train an RF classifier to predict PoL labels at each timestamp.
- **CNN:** We train a three-layer convolutional neural network (CNN) that takes the positional sequences as input and generates a sequence of PoL labels.
- **TS2Vec:** [32] TS2Vec is a universal time-series representation learning model. We apply its encoder module to learn the representation of the positional sequences.

5.3 Overall accuracy

Quantitative Analysis Table 2 presents a comprehensive performance comparison of various methods in both the EW and NS directions using the F1 score at different thresholds (10, 25, 50), edit score, and accuracy. Generally, all methods perform better in the NS direction than in the EW direction, because the EW direction contains five types of PoL, while the NS direction only contains four. The proposed method, DiffPoL, and Expert-ML achieved similar performance, indicating that the proposed method can achieve performance comparable to complex rules in an end-to-end manner, eliminating the dependence on domain expert knowledge. DiffPoL shows superior performance across all metrics compared to other baselines. Especially for segment and sequence-level metrics, DiffPoL achieves steady and accurate performance with F1 and edit scores above 90% in both directions. Although some baseline methods, such as TS2Vec and RF, achieved accurate point-wise accuracy, their performance at the segment and sequence level was poor, with F1 and edit scores ranging from 30% to 70%. Heuristic and CLaSP performed poorly in all metrics, indicating that those universal methods are not directly capable of PoL identification. These significant scores highlight the effectiveness of DiffPoL in handling complex satellite positional data and refining the identification process, thereby achieving accurate and reliable PoL identification.

Visualization Analysis Fig. 6 visualizes the identification results of 10 randomly selected objects in EW direction compared to the ground truth. The identification results

²<https://github.com/yeyongchao/satellite-PoL-diffusion>

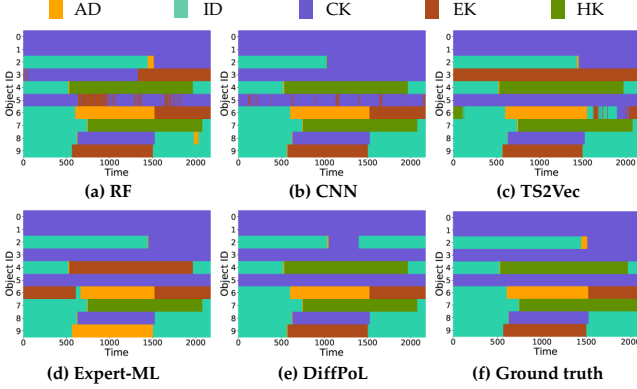


Figure 6. Visualization of identification results in EW direction. (a-c) Identifications are fragmented at transition boundaries. (d,e) Identifications are clear and structured, but (d) is less accurate.

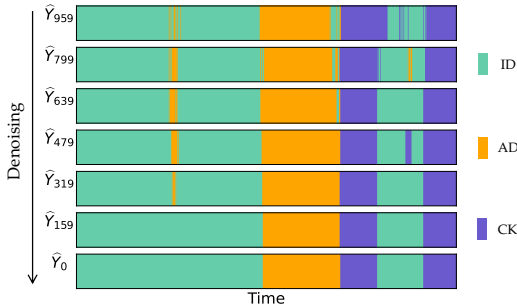


Figure 7. Visualization of the denoising process.

of RF, CNN and TS2Vec, Fig. 6 (a-c), although achieving high point-wise accuracy, are fragmented, particularly at the boundaries of different states, leading to unnecessary segmentation. Such fragmentation often requires manual refinement, which is labor-intensive and time-consuming. DiffPoL, as well as Expert-ML, shows clear and structured identification sequences, as shown in Fig. 6 (d,e). These structured identifications are practicable for further analysis and can be directly used for downstream applications. The visualization results, consistent with the quantitative analysis of F1 and edit scores, highlight the superiority of DiffPoL in identifying satellite PoL in an end-to-end manner without the need for further refinement of the sequence identification results. The visualization shows a similar pattern for NS direction can be found in **Appendix D.1**.

We further select an object and visualize its denoising process at different steps in Fig. 7, where different color represent different PoL labels. From \hat{Y}_{959} to \hat{Y}_0 , is the beginning to end of the denoising process. It can be observed that, at the beginning of the denoising process, \hat{Y}_{959} , the sequence is heavily noisy and fragmented with many misclassifications. As the denoising process progresses, the identification gradually becomes clearer and more structured, particularly the

fluctuations at the boundaries of different states are gradually refined. This is consistent with the quantitative results, where such a refinement process significantly reduces unnecessary segmentation, improving identification in sequence-level and showing a significant improvement in F1 and edit scores. This visualization demonstrates the effectiveness of the denoising process in refining the sequence to achieve accurate PoL identification, which aligns well with the motivation of applying the diffusion process in DiffPoL.

5.4 Generality of DiffPoL

As illustrated in Fig. 5, satellite positions are not always consistently observed in practice due to various factors such as signal transmission issues and different monitoring requirements in different orbits, which poses a significant challenge when deploying satellite PoL algorithms in real-world scenarios. Thus, in this section, we further evaluate the utility of DiffPoL with satellite positional sequences that have low sampling rates. Fig. 8 shows the identification performance comparison across different methods under original and low sampling rates in EW direction. Specifically, while the performance of other methods, such as RF, drops noticeably under low sampling rates, DiffPoL remains steady and robust. Expert-ML and DiffPoL show similar high performance under the original sampling rate, with F1 scores close to 90. However, under the low sampling rate, Expert-ML’s performance drops significantly, with F1 scores falling to around 60, while DiffPoL maintains a relatively steady performance with F1 scores remaining above 80. The significant drop of Expert-ML is likely due to its rule-based nature, which makes it more sensitive to variations in sampling intervals, indicating its limitation across low sampling rate scenario. In contrast, DiffPoL’s design allows it to handle the challenges posed by irregular sampling intervals effectively. Similar trends were observed in the NS direction, confirming the method’s robustness across different sampling rate (see **Appendix D.2** for details).

We further select an object and visualize its identification results in EW direction with different sampling rate data in Fig. 9. TS2Vec, Expert-ML, and DiffPoL are selected as the comparison. The results of Expert-ML show considerable deviation from the ground truth, indicating its sensitivity to low sampling rates. In contrast, DiffPoL maintains consistent performance, closely matching the ground truth. TS2Vec, due to its convolutional kernel-based design, shows stable performance in point-wise labeling but still exhibits fragmentation issues at state boundaries. These observations highlight the effectiveness of DiffPoL in handling positional sequences with low sampling rates, making it a more reliable choice for PoL identification for online operation scenarios.

6 Related Work

Satellite PoL identification Current practices in satellite PoL identification are still in their developmental stages,

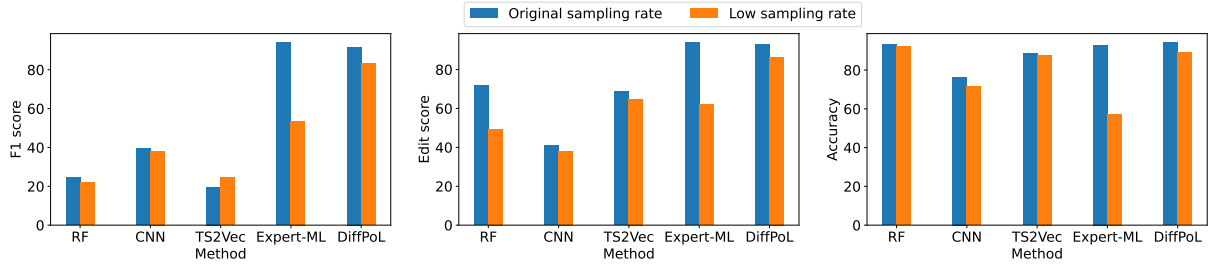


Figure 8. Identification performance comparison with different sampling rates in EW direction.

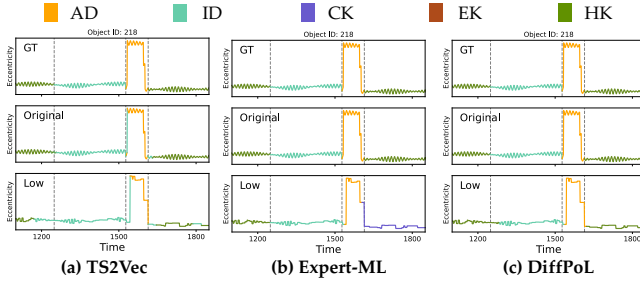


Figure 9. Visualization of identification results with different sampling rate data in EW direction. Top to bottom: Ground truth, results with original sampling rate, results with low sampling rate.

heavily relying on extensive expert knowledge [12, 14, 18, 37]. For example, Stijn *et al.* detected anomalies in low earth orbit satellite positions through consistency checks between the two-line element (TLE) sets and used background models. Similarly, Roberts *et al.* utilized longitude to identify geosynchronous satellite maneuvers [18]. These methods, based on rule-based approaches or statistical, are labor-intensive due to the growing volume of daily operational data, limiting their scalability with the increasing number of satellites to track and their applicability across different satellites and systems. A few studies that leverage deep learning techniques for PoL identification have been reported. Roberts *et al.* first used convolutional neural networks to detect longitudinal shift maneuvers in geosynchronous satellites [19] and then advanced the method with k-means clustering [20] and extended validation [22]. However, the outputs of these models often require further refinement to produce a usable PoL sequence.

Time-series segmentation Time-series segmentation involves dividing a sequence into meaningful segments for analysis, sharing similarities with tasks such as change point detection and anomaly detection [33]. Various methods, ranging from statistical techniques to advanced deep learning approaches, can be grouped into universal and domain-specific methods. Universal methods are based on unsupervised or self-supervised change point detection [1, 2, 4, 6]. For example, CLaSP hierarchically splits the series by training binary classifiers at each potential split point [4], while PaTSS detects gradual state transitions by learning a distribution over

semantic segments from an embedding space derived from mined sequential patterns [1]. However, these methods cannot utilize labels for learning, which limits their performance. Some domain-specific methods have been developed, especially for human health and activity-related tasks. For example, Perslev *et al.* proposed U-Time, a convolutional network based on the U-Net architecture for sleep stage classification [17], and Xia *et al.* segmented wearable-based activity sensor data using contrastive learning and order-preserving optimal transport [29]. These methods are customized according to specific data, making them difficult to apply directly to cross-domain tasks like PoL identification.

Temporal action segmentation In the context of computer vision, temporal action segmentation, tagging each video frame with a corresponding action label, shares similarities with PoL identification in terms of sequence segmentation. Several innovative approaches have been developed to address this task [3]. One notable method is the use of diffusion models for action segmentation, as proposed by Liu *et al.* [16]. This approach utilizes diffusion models to iteratively generate action predictions from random noise, conditioned on input video features. Some studies have focused on leveraging temporal consistency for action segmentation, such as multi-stage refinement [5, 13], unsupervised optimal transport [30]. These recent advancements highlight the continuous evolution and innovation in temporal action segmentation, providing valuable insights for satellite PoL identification.

7 Conclusion

This paper presents a novel diffusion-based method, DiffPoL, for the identification of satellite pattern-of-life (PoL), addressing significant challenges posed by the complexity and variability of aerospace systems. By utilizing a multivariate time-series encoder and a tailored decoder within a diffusion model, DiffPoL achieves end-to-end PoL identification in a sequence PoL label generation manner, which is the first exploration of end-to-end PoL identification with diffusion models. Experiments on real-world satellite positional datasets prove DiffPoL can identify satellite PoL in an end-to-end without the need for manual refinement or

domain-specific feature engineering. Comparison over state-of-the-art methods demonstrates the superiority of DiffPoL, especially in sequence-level evaluation. Additionally, DiffPoL is robust to the variations in the sampling rate of satellite observation data, making it more applicable to real-world scenarios. This novel approach not only enhances the scalability and applicability of PoL identification but also contributes to improved space situational awareness and satellite monitoring. For future work, we aim to explore the application of DiffPoL on a broader range of satellites and aerospace systems.

References

- [1] Louis Carpentier, Len Feremans, Wannes Meert, and Mathias Verbeke. 2024. Pattern-based Time Series Semantic Segmentation with Gradual State Transitions. In *Proceedings of the 2024 SIAM International Conference on Data Mining, SDM 2024, Houston, TX, USA*. 316–324.
- [2] Shohreh Deldari, Daniel V. Smith, Hao Xue, and Flora D. Salim. 2021. Time Series Change Point Detection with Self-Supervised Contrastive Predictive Coding. In *WWW '21: The Web Conference 2021, Virtual Event / Ljubljana, Slovenia*. 3124–3135.
- [3] Guodong Ding, Fadime Sener, and Angela Yao. 2024. Temporal Action Segmentation: An Analysis of Modern Techniques. *IEEE Transactions on Pattern Analysis and Machine Intelligence* 46, 2 (2024), 1011–1030.
- [4] Arik Ermshaus, Patrick Schäfer, and Ulf Leser. 2023. ClaSP: parameter-free time series segmentation. *Data Min. Knowl. Discov.* 37, 3 (2023), 1262–1300.
- [5] Yazan Abu Farha and Jurgen Gall. 2019. MS-TCN: Multi-stage temporal convolutional network for action segmentation. In *Proceedings of the IEEE/CVF conference on computer vision and pattern recognition*. 3575–3584.
- [6] Shaghayegh Gharghabi, Yifei Ding, Chin-Chia Michael Yeh, Kaveh Kamgar, Liudmila Ulanova, and Eamonn J. Keogh. 2017. Matrix Profile VIII: Domain Agnostic Online Semantic Segmentation at Superhuman Performance Levels. In *2017 IEEE International Conference on Data Mining, ICDM 2017, New Orleans, LA, USA*. 117–126.
- [7] Shansan Gong, Mukai Li, Jiangtao Feng, Zhiyong Wu, and LingPeng Kong. 2022. Diffuseq: Sequence to sequence text generation with diffusion models. *arXiv preprint arXiv:2210.08933* (2022).
- [8] Jonathan Ho, Ajay Jain, and Pieter Abbeel. 2020. Denoising diffusion probabilistic models. *Advances in Neural Information Processing Systems* 33 (2020), 6840–6851.
- [9] Jonathan Ho and Tim Salimans. 2022. Classifier-free diffusion guidance. *arXiv preprint arXiv:2207.12598* (2022).
- [10] XuXing Huang, Bin Yang, Shuang Li, and ZhenBo Wang. 2021. Efficient high-accuracy north-south station-keeping strategy for geostationary satellites. *Science China Technological Sciences* 64, 11 (2021), 2415–2426.
- [11] Byoung-Sun Lee, Jeong-Sook Lee, and Kyu-Hong Choi. 1999. Analysis of a station-keeping maneuver strategy for collocation of three geostationary satellites. *Control Engineering Practice* 7, 9 (1999), 1153–1161.
- [12] Stijn Lemmens and Holger Krag. 2014. Two-line-elements-based maneuver detection methods for satellites in low earth orbit. *Journal of Guidance, Control, and Dynamics* 37, 3 (2014), 860–868.
- [13] Shijie Li, Yazan Abu Farha, Yun Liu, Ming-Ming Cheng, and Jurgen Gall. 2023. MS-TCN++: Multi-Stage Temporal Convolutional Network for Action Segmentation. *IEEE transactions on pattern analysis and machine intelligence* 45, 6 (2023), 6647–6658.
- [14] Tao Li and Lei Chen. 2018. Historical-orbital-data-based method for monitoring the operational status of satellites in low Earth orbit. *Acta Astronautica* 151 (2018), 88–94.
- [15] Zhenghao Lin, Yeyun Gong, Yelong Shen, Tong Wu, Zhihao Fan, Chen Lin, Nan Duan, and Weizhu Chen. 2023. Text generation with diffusion language models: A pre-training approach with continuous paragraph denoise. In *International Conference on Machine Learning*. 21051–21064.
- [16] Daochang Liu, Qiyue Li, Anh-Dung Dinh, Tingting Jiang, Mubarak Shah, and Chang Xu. 2023. Diffusion Action Segmentation. In *IEEE/CVF International Conference on Computer Vision, ICCV 2023, Paris, France*.
- [17] Mathias Perslev, Michael Hejlsbak Jensen, Sune Darkner, Poul Jørgen Jennum, and Christian Igel. 2019. U-Time: A Fully Convolutional Network for Time Series Segmentation Applied to Sleep Staging. In *Advances in Neural Information Processing Systems 32: Annual Conference on Neural Information Processing Systems 2019, NeurIPS 2019*. 4417–4428.
- [18] TG Roberts and R Linares. 2020. Satellite repositioning maneuver detection in geosynchronous orbit using two-line element (TLE) data. In *71st International Astronautical Congress*.
- [19] Thomas G Roberts and Richard Linares. 2021. Geosynchronous satellite maneuver classification via supervised machine learning. In *Advanced Maui Optical and Space Surveillance Technologies Conference, Maui, Hawaii*.
- [20] Thomas G Roberts, Haley E Solera, and Richard Linares. 2023. Geosynchronous satellite behavior classification via unsupervised machine learning. In *9th Space Traffic Management Conference, Austin, TX, Vol. 3*.
- [21] Peng Mun Siew, Haley E Solera, Thomas G Roberts, Daniel Jang, Victor Rodriguez-Fernandez, Jonathan P How, and Richard Linares. 2023. AI SSA Challenge Problem: Satellite Pattern-of-Life Characterization Dataset and Benchmark Suite. In *Proceedings of the Advanced Maui Optical and Space Surveillance (AMOS) Technologies Conference, Maui, Hawaii*, 5.
- [22] Haley E Solera, Thomas G Roberts, and Richard Linares. 2023. Geosynchronous satellite pattern of life node detection and classification. In *9th Space Traffic Management Conference, Austin, TX*.
- [23] Jiaming Song, Chenlin Meng, and Stefano Ermon. 2020. Denoising diffusion implicit models. *arXiv preprint arXiv:2010.02502* (2020).
- [24] Statista. 2024. Number of cataloged, decayed, and on orbit satellite objects worldwide from 1958 to 2023. <https://www.statista.com/statistics/1422809/number-of-satellites-cataloged-decayed-orbit/>.
- [25] Ashish Vaswani, Noam Shazeer, Niki Parmar, Jakob Uszkoreit, Llion Jones, Aidan N Gomez, Łukasz Kaiser, and Illia Polosukhin. 2017. Attention is all you need. *Advances in neural information processing systems* 30 (2017).
- [26] Michael JH Walker, B Ireland, and Joyce Owens. 1985. A set modified equinoctial orbit elements. *Celestial mechanics* 36, 4 (1985), 409–419.
- [27] Michael JH Walker, B Ireland, and Joyce Owens. 1985. A set modified equinoctial orbit elements. *Celestial mechanics* 36, 4 (1985), 409–419.
- [28] Haomin Wen, Youfang Lin, Yutong Xia, Huaiyu Wan, Qingsong Wen, Roger Zimmermann, and Yuxuan Liang*. 2023. DiffSTG: Probabilistic Spatio-Temporal Graph Forecasting with Denoising Diffusion Models. In *Proceedings of the 31st International Conference on Advances in Geographic Information Systems*.
- [29] Songpengcheng Xia, Lei Chu, Ling Pei, Jiarui Yang, Wenxian Yu, and Robert C. Qiu. 2023. Timestamp-supervised Wearable-based Activity Segmentation and Recognition with Contrastive Learning and Order-Preserving Optimal Transport. *arXiv abs/2310.09114* (2023).
- [30] Ming Xu and Stephen Gould. 2024. Temporally Consistent Unbalanced Optimal Transport for Unsupervised Action Segmentation. In *Proceedings of the IEEE/CVF Conference on Computer Vision and Pattern Recognition*. 14618–14627.
- [31] Ling Yang, Zhilong Zhang, Yang Song, Shenda Hong, Runsheng Xu, Yue Zhao, Yingxia Shao, Wentao Zhang, Bin Cui, and Ming-Hsuan Yang. 2022. Diffusion models: A comprehensive survey of methods and applications. *arXiv preprint arXiv:2209.00796* (2022).
- [32] Zhihan Yue, Yujing Wang, Juanyong Duan, Tianmeng Yang, Congrui Huang, Yunhai Tong, and Bixiong Xu. 2022. Ts2vec: Towards universal representation of time series. In *Proceedings of the AAAI Conference on Artificial Intelligence*, Vol. 36. 8980–8987.
- [33] Kexin Zhang, Qingsong Wen, Chaoli Zhang, Rongyao Cai, Ming Jin, Yong Liu, James Y Zhang, Yuxuan Liang, Guansong Pang, Dongjin Song, et al. 2024. Self-supervised learning for time series analysis: Taxonomy, progress, and prospects. *IEEE Transactions on Pattern Analysis and Machine Intelligence* (2024).
- [34] Lvmin Zhang, Anyi Rao, and Maneesh Agrawala. 2023. Adding conditional control to text-to-image diffusion models. In *Proceedings of the IEEE/CVF International Conference on Computer Vision*. 3836–3847.

- [35] Yuanshao Zhu, Yongchao Ye, Shiyao Zhang, Xiangyu Zhao, and James Yu. 2023. DiffTraj: Generating GPS Trajectory with Diffusion Probabilistic Model. In *Annual Conference on Neural Information Processing Systems 2023, NeurIPS 2023, New Orleans, LA, USA*.
- [36] Yuanshao Zhu, James Jianqiao Yu, Xiangyu Zhao, Qidong Liu, Yongchao Ye, Wei Chen, Zijian Zhang, Xuetao Wei, and Yuxuan Liang. 2024. ControlTraj: Controllable Trajectory Generation with Topology-Constrained Diffusion Model. In *Proceedings of the 30th ACM SIGKDD Conference on Knowledge Discovery and Data Mining*.
- [37] Andrea Zollo and Martin Weigel. 2024. Comparison of satellite manoeuvre detection methods based on timeline of orbit elements. *Advances in Space Research* 73, 1 (2024), 286–303.

A Details on Expert-ML Method

In this section, we provide a comprehensive implementation of PoL identification baseline method with domain knowledge. Fig. 10 illustrates its workflow, differentiating the processes for east-west (EW) and north-south (NS) directions due to their independent operations and disparate label distributions. Specifically, the workflow for each direction includes: 1) identifying the label of two distinct behavior modes: station-keeping (SK) and drift, 2) for EW direction, further distinguishing between adjust drift (AD) and initial drift (ID), and 3) identifying the specific propulsion types, i.e., chemical keeping (CK), electric keeping (EK), and hybrid keeping (HK). Rule-based methods and data-driven methods are for these tasks in each direction. Additionally, results from EW and NS directions are cross-verified to refine the final identifications and address any exceptional cases.

A.1 East-west (EW) direction

A.1.1 EW drift identification. To identify EW drift labels, a rule-based method is formulated based on the empirical observations. The observation indicates that drift in the EW direction is characterized by variations in longitude, eccentricity, and semi-major axis, which correspond closely with the goals of EW station-keeping (SK) maneuvers, aimed at keeping the orbital period perfectly synchronous with the Earth rotation and ensuring minimal eccentricity [11]. Specifically, AD records the transition between different drift states, evidenced by significant changes in longitude drift rate or changes in drift direction in longitude, often paired with step changes in eccentricity and semi-major axis. In contrast, ID marks the satellite’s transition from SK to drift phase. Two distinct patterns of ID in the EW direction are noted: one resembling AD’s characteristics, and another displaying a gradual longitudinal drift without step changes in eccentricity or semi-major axis.

Accordingly, the time index for EW drift labels is determined by identifying points of step change in eccentricity. The type of drift is then classified based on the satellite’s state transition around the drift timestamp. Specifically, if the transition indicates a shift from SK to drift, it is categorized as ID; otherwise, it is recognized as AD. However, this rule does not entirely encompass all EW drift labels. Notably,

there are exceptional instances of EW-ID that do not exhibit step changes in eccentricity. These anomalies are further investigated in **Appendix A.3**.

A.1.2 EW station keeping identification. Due to the diverse behavioral patterns exhibited by SK modes, which vary according to the type of propulsion utilized, more than rule-based methods are required to identify keeping labels. Thus, a data-driven approach is applied to identify EW SK labels. This method utilizes orbit elements over specific time slices to train a machine-learning model capable of pinpointing the behavioral mode. For EW SK, the critical orbital elements are eccentricity e , semi-major axis Ω , and argument of periapsis ω [26]. To capture the periodicity in the EW direction, a sliding window technique is employed, featuring a duration of 24 hours and a step interval of 2 hours. Initially, a binary classifier is trained to ascertain whether each time slice represents SK or drift. Upon detecting a step change in output from drift to SK, this transition is marked as an SK transition, thus determining the time index. Following the identification of an SK transition, a three-class classifier is then employed to specify the type of SK. The same methodology applies to the identification of the start of the study period (SS) labels, where the binary classifier first determines whether the state is non-keeping (NK) or SK, and subsequently, the three-class classifier elaborates on the type of SK.

A.2 North-south (NS) direction

A.2.1 NS drift identification. Similar to the methods for the EW direction, rule-based methods are developed for NS drift labels. NS direction maneuvers primarily adjust the inclination of the satellite. NS-ID represents a transition from an SK state to a drift state, signifying the termination of SK maneuvers. However, it is noted that NS-ID labels are not consistently placed at the time index where a feature change occurs. There are two observed patterns of NS-ID in the training data: In some instances, the NS-ID is labeled concurrently with the EW-ID. Since no distinctive changes are observed in related orbital elements in these instances, it is assumed that the NS-ID’s time index is determined by the corresponding EW-ID. In other cases, the NS-ID does not align with the EW-ID. Here, the NS-ID time index is positioned at the timestamp where the next SK maneuver would have been expected had the satellite remained in an SK state.

Accordingly, two rules are proposed for identifying NS-ID labels. First, if an EW-ID is identified, and there is a concurrent transition from SK to drift in the NS direction, the NS-ID is marked with the same time index as the EW-ID. Second, suppose NS-ID is not correlated with the EW-ID. In that case, it is marked based on the expected timing of the next SK maneuver, adhering to the periodicity characteristic of the type of SK being employed. Specifically, our findings

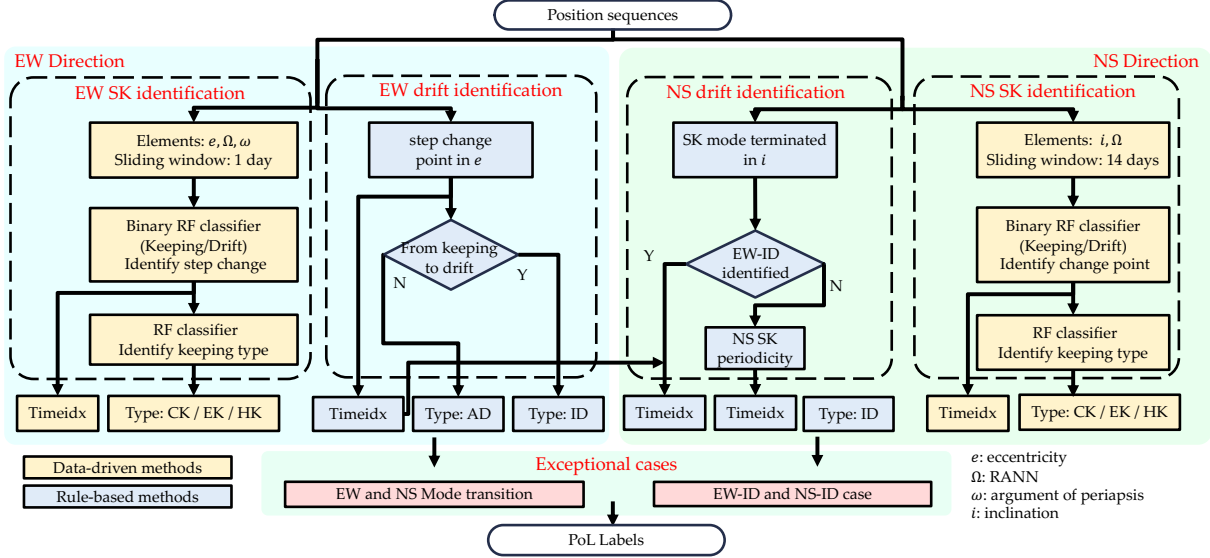


Figure 10. The workflow of the proposed Expert-ML.

indicate that the periodicity varies by SK type, i.e., 14 days for CK, 7 or 5 days for HK, and 1 day for EK.

A.2.2 NS station keeping identification. For NS SK, we follow the same workflow as EW SK, wherein a binary classifier is trained to pinpoint the time index, and a subsequent three-class classifier is deployed to determine the SK type. The difference lies in the feature engineering. Behavior and periodicity in the NS direction can be understood through a projection in equinoctial coordinates, specifically using $q = \tan(i/2) \cdot \cos(\Omega)$, $p = \tan(i/2) \cdot \sin(\Omega)$ [27]. Consequently, we select p, q , derived from by i, Ω , as features for the classifier. The sliding window size is set to 14 days to cover the periodicity of all SK types.

A.3 Exceptional cases

After identifying labels in both EW and NS directions, we refine these identifications based on observed patterns.

1) *Mode transition*: Observations reveal distinct patterns in mode transitions for both directions. In the NS direction, a cyclical pattern between IK and ID is evident, whereas in the EW direction, the sequence typically progresses from ID to AD to IK. Notably, aside from AD, labels do not repeat the same mode within a sequence. Moreover, while a satellite maintains the same SK type in a given direction, it may exhibit different SK types between the EW and NS directions. Consequently, we refine identifications in both directions by eliminating redundant SK labels and verifying the consistency of the SK type within the same directional axis.

2) *EW-ID and NS-ID case*: As previously mentioned, certain EW-ID labels pose challenges for identification using existing rules. Furthermore, in the training data, these specific EW-ID

labels consistently co-occur with NS-ID labels. Consequently, we employ a binary classifier to determine the time index for these cases, utilizing a methodology similar to those used for identifying SK time indices in both EW and NS directions. The classifier leverages selected orbital elements from both directions as input features.

A.4 Limitation discussion

Although the Expert-ML method can achieve practical PoL identification, it has limitations in algorithm design and actual application. 1) Rules are defined based on observations from the data and expert knowledge, which need to be manually updated when applied to different satellites. 2) Despite using some data-driven methods, these simple machine learning models rely on feature engineering, which is based on expert knowledge. The design of feature engineering may vary for different satellites. 3) Since neither rule-based nor data-driven methods can directly achieve satisfactory PoL identification, complex rules are defined to refine outputs from different methods. This process is labor-intensive and cannot be generalized to other scenarios. 4) In practice, the Expert-ML method is sensitive to the sampling rate of satellite position data, especially for those rules defined based on step changes. Detailed performance of Expert-ML method can refer to Table 2 and Figure 11.

B Experimental Setups

In this section, we provide details of experimental setups, including evaluation metrics definitions and baseline implementation details.

B.1 Evaluation Metrics

To fully evaluate the quality of PoL identification, we follow the practice in sequence segmentation tasks [3, 16], and use three evaluation metrics at different levels. Specifically, let Y be the ground truth label sequence and \hat{Y} be the output of the model, the metrics are defined as follows:

Accuracy (Acc): Accuracy is a point-wise metric that measures the proportion of correctly identified PoL labels out of the total labels.

$$\text{Acc} = \frac{\sum_{i=1}^n \mathbb{I}(Y_i = \hat{Y}_i)}{n} \times 100\%, \quad (10)$$

where $\mathbb{I}(\cdot)$ is the indicator function that equals 1 when the condition is true and 0 otherwise, and n is the total number of labels.

Edit score (Edit): The edit score is a sequence-level metric that quantifies the similarity between two sequences based on the Levenshtein distance, which is the minimum number of actions required to transform one sequence into another. The accumulated distance value $e_{i,j}$ is defined as:

$$e_{i,j} = \begin{cases} \max(i, j), & \text{if } \min(i, j) = 0 \\ \min(e_{i-1,j} + 1, e_{i,j-1} + 1, & \text{otherwise} \\ e_{i-1,j-1} + \mathbb{I}(Y_i \neq \hat{Y}_j)) & \end{cases} \quad (11)$$

Then, the edit score is normalized by the maximum length of the two sequences:

$$\text{Edit} = \left(1 - \frac{e[|Y|, |\hat{Y}|]}{\max(|Y|, |\hat{Y}|)}\right) \times 100\%. \quad (12)$$

F1-score (F1): F1-score is a segment-level metric that compares the Intersection over Union (IoU) of each segment with respect to the corresponding ground truth based on a threshold τ . A segment is considered a true positive if its IoU with respect to the ground truth exceeds the threshold. If there is more than one correct segment within the span of a single ground truth action, only one segment is considered a true positive, and the others are marked as false positives. Based on the true and false positives, as well as false negatives (missed segments), the precision and recall are computed:

$$\begin{aligned} \text{Precision} &= \frac{\sum_{i=1}^n \mathbb{I}(Y_i = \hat{Y}_i \text{ and } \hat{Y}_i = 1)}{\sum_{i=1}^n \mathbb{I}(\hat{Y}_i = 1)} \\ \text{Recall} &= \frac{\sum_{i=1}^n \mathbb{I}(Y_i = \hat{Y}_i \text{ and } Y_i = 1)}{\sum_{i=1}^n \mathbb{I}(Y_i = 1)} \end{aligned} \quad (13)$$

and the F1-score is computed as the harmonic mean of precision and recall. Follow common practices [3, 16], we set the threshold τ to 0.1, 0.25, 0.5, respectively.

C Ablation study

To investigate the contribution of each sub-module to the overall performance of DiffPoL, we carry out comprehensive experiments with the following ablated variants:

Table 3. Performance comparison of ablated models in EW direction. (Original / Low sampling rate)

Ablated models	F1 (%) @ {10} (↑)	Edit (%) (↑)	Acc (%) (↑)
w/o decoder	41.11 / 12.99	85.92 / 47.93	94.37 / 87.78
w/o geodetic	87.30 / 75.70	87.53 / 80.38	91.58 / 83.08
w/o Sloss	85.06 / 72.49	87.64 / 76.91	92.82 / 83.68
w/o mask	91.09 / 78.07	91.61 / 83.51	93.14 / 85.14
DiffPoL	91.68 / 83.15	93.00 / 86.41	94.10 / 88.91

Table 4. Performance comparison of ablated models in NS direction. (Original / Low sampling rate)

Ablated models	F1 (%) @ {10} (↑)	Edit (%) (↑)	Acc (%) (↑)
w/o decoder	57.21 / 29.21	86.72 / 60.90	98.44 / 96.25
w/o geodetic	94.69 / 89.69	95.84 / 88.53	98.62 / 94.92
w/o Sloss	83.32 / 72.14	90.08 / 81.46	95.54 / 92.41
w/o mask	92.72 / 86.48	95.56 / 88.07	98.97 / 96.60
DiffPoL	94.79 / 92.69	96.72 / 93.11	98.20 / 96.59

- **w/o decoder:** The decoder module is removed, only the encoder is trained with cross-entropy loss.
- **w/o geodetic:** The model takes only the six Keplerian elements as input, excluding the geodetic features, i.e., latitude, longitude, and altitude.
- **w/o Sloss:** The segment-level losses introduced in Sec. 4.3 are removed. The model is trained only with the cross-entropy loss.
- **w/o mask:** The mask strategy mentioned in Sec. 4.3 is removed.

Table 3 shows the performance comparison of the ablated models in EW direction under both original and low sampling rates. Results show that when removing the decoder, the model behaves similarly to other data-driven baselines and shows limited performance at the segment and sequential levels. This further underscores the crucial role of the denoising process in refining the sequence to achieve accurate identification. For other ablated models, although the performance gap compared to DiffPoL is not as significant as w/o decoder, there is still a noticeable decline, indicating that each sub-module contributes to the overall performance. In particular, removing segment-level losses (w/o Sloss) leads to a significant drop in F1 and edit scores, highlighting the importance of the segment-level supervision mechanism in guiding the model to learn the sequential patterns effectively. The mask strategy (w/o mask) shows a more noticeable impact on low sampling rates than the original sampling rate. As EW maneuvers show patterns in longitude, the geodetic features (w/o geodetic) also play a crucial role in enhancing the model’s performance. Similar trends were observed in the NS direction (see Table 4).

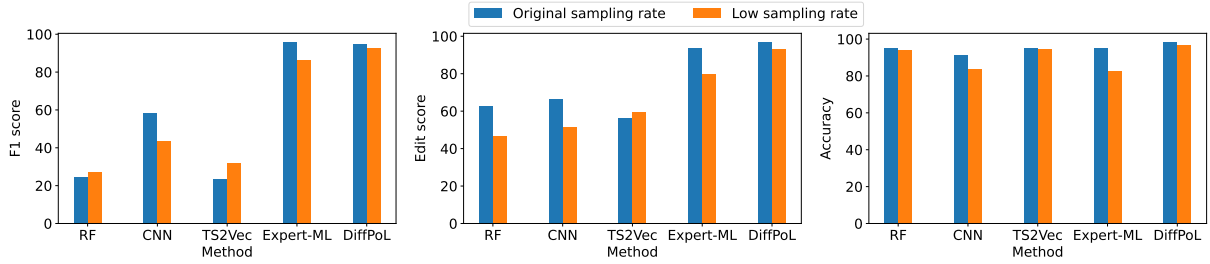


Figure 11. Identification performance comparison with different sampling rates on the NS direction.

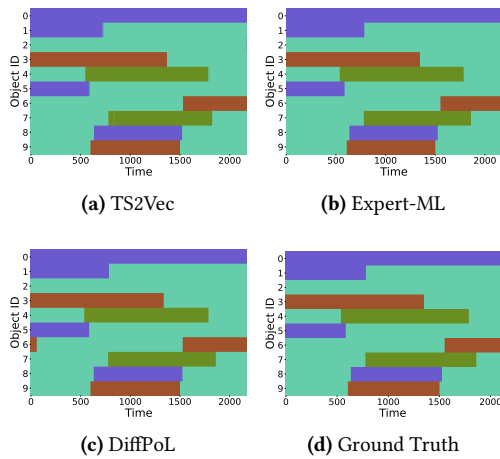


Figure 12. Visualization of identification results in NS direction. Different colors represent different categories of PoL labels.

D Results on North-South direction

In this section, we provide extra experimental results in NS direction to support the main results in the paper.

D.1 Visualization results

Fig. 12 visualizes the identification results in NS direction for different methods compared to the ground truth.

D.2 Generality results

Fig. 11 shows the identification performance comparison across different methods under original and low sampling rates in NS direction.